NJC

PAPER

View Article Online
View Journal

Cite this: DOI: 10.1039/c9nj04290c

A polyaniline-coated ZnS/ZnO/FTO photoelectrode for improving photocorrosion prevention and visible light absorption†

Hyun Kim and Bee Lyong Yang *

Received 19th August 2019,
Accepted 5th October 2019

DOI: 10.1039/c9nj04290c

rsc.li/njc

To enhance the absorption of visible light for wide-bandgap semiconductors, methods such as sensitizing with nanoparticles or quantum dots and bandgap engineering using dopants have been reported. However, these can cause lattice mismatch, inherent disorder, or imperfect charge balance, which serve as recombination sites and significantly reduce the photocatalytic efficiency. Herein, photoelectrodes of polyaniline (PANI)/ZnS/ZnO on F:SnO_2 (FTO) were fabricated to evaluate these issues and examine their interface microstructural and photocatalytic properties. The PANI films were applied as a visible light sensitizer and photocorrosion prevention layer for ZnS/ZnO. Subsequently, the photocurrent loss effect due to photocorrosion was systematically investigated. The photocurrent of the PANI/ZnS/ZnO photoelectrode measured at 0.5 V under white light illumination was approximately five times higher than that of the ZnO nanorod photoelectrode. This was attributed to photocorrosion prevention and visible light absorption by the PANI layers, due to proper energy band alignment of the hybrid heterojunction semiconductors.

Introduction

Clean hydrogen evolution technology has attracted attention for several decades because hydrogen is the renewable energy source of the future in a hydrogen energy based society. Despite currently available hydrogen evolution techniques such as reforming of natural gas, electrolysis of water, and biomass conversion, commercialization of hydrogen evolution by solar water splitting as the ultimate clean energy source is being currently studied around the world.[1–8] The solar energy received by the earth consists of ultraviolet (~5%) and visible light (~43%). Nanostructures are important not only for visible-light absorption in the solar spectrum, but also to obtain a high photocatalytic efficiency for semiconductor photoelectrodes. There has been extensive research on various nanostructured photoelectrodes such as nanowires, nanorods, and nanotubes.[9–14] Many multilayered heterojunction nanostructures with great penetration depth have also been reported for the absorption of longer wavelengths of visible light as well as for efficient charge separation and transfer of excited electrons and holes.[15–18]

Among the methods to enhance visible-light absorption is to adhere inorganic semiconductors with narrow-bandgap materials such as nanoparticles or quantum dots (QDs) on the surface of wide-bandgap semiconductors, as sensitizers.[19–21] Another way is to manipulate the bandgap sufficiently to obtain a visible light spectrum response of 1.7–2.9 eV by doping impurities such as carbon, nitrogen, or hydrogen.[22,23] Regarding visible-light sensitizers, studies on chalcogenide compound QDs such as CdS (E_g = 2.4 eV), CdSe (1.7 eV), and CdSSe (1.9 eV) have been reported,[24] as well as those on plasmonic Ag and Au nanoparticles,[25] transition metal dichalcogenide sheets such as MoS_2 and WS_2,[26] and metal halide perovskites such as $CH_3NH_3PbI_3$ and $CsPbBr_3$.[27] However, it is important to develop alternative sensitizer materials, owing to significant disadvantages of the above-mentioned materials, such as the harmful nature of Cd, the high cost of noble metals, and instability in the presence of moisture. In bandgap engineering through doping of single or several impurities, the recombination probability of excited electrons and holes is very high near doping sites, which include deteriorative crystal defects such as lattice mismatch at the interface between the sensitizers and wide-bandgap semiconductors, unstable inherent disorder,[28] and charge imbalance among dopants. Hence, even though the absorption of visible light is improved by doping, these recombination sites can cause significant loss of photocatalytic current during the separation and transfer of electrons and holes excited by visible light. Meanwhile, there are a few reports on the photocorrosion of sensitizers such as QDs and nanoparticles attached on wide-bandgap semiconductors or that of semiconductors themselves.[29–31] As alternatives, polymeric

School of Materials Science and Engineering, Kumoh National Institute of Technology, 61 Daehak-ro, Gumi-si, Gyeongsangbuk-do 39177, Republic of Korea. E-mail: blyang@kumoh.ac.kr

† Electronic supplementary information (ESI) available. See DOI: 10.1039/c9nj04290c

materials have recently been proposed as a prevention layer for photocorrosion.[32,33] PANI has been reported as a conducting polymer able to absorb visible light, and a few studies of its photocorrosion prevention effect have been reported.[34] However, systematic studies on the photocatalytic performance using these films have not been reported thus far.

In this study, conductive organic polyaniline (PANI, $\Delta E_{LUMO-HOMO}$ = 2.4 eV) was applied with core/shell composites of ZnS film/ZnO nanorods (NRs) on F:SnO_2 (FTO) substrates. Subsequently, the performance of PANI as a sensitizer as well as a prevention layer to improve the photocatalytic properties is evaluated. To fabricate the hybrid core/shell heterojunction photoelectrodes, after ZnO NRs were grown on the FTO substrates by electrodeposition, ZnS films were formed on the surface of the ZnO NRs by chemical dipping of the ZnO NRs into Na_2S solution. Finally, PANI films were applied as a coating by chemical dipping techniques. A ZnO semiconductor with a direct bandgap generally causes low heat loss of the absorbed energy and smoothly transfers photoexcited electrons and holes, due to dipoles of stacked Zn^{2+} cations and O^{2-} anions in the crystal. Hence, as long as the visible light absorbance in ZnO is improved, almost all excited carriers can directly contribute to the photocatalytic efficiency.

Meanwhile, a ZnO seed layer is necessary to grow vertical hexagonal ZnO NRs on the surface of tetragonal FTO, and also to reduce the lattice mismatch between ZnO and FTO during the hydrothermal process. However, this growth is possible without a seed layer if electrodeposition is employed. Electrodeposited ZnO NRs also provide a stable interface on FTO surfaces,[35–38] so that photoexcited electrons and holes can be smoothly transferred through the interfaces between the ZnO NRs and FTO. The conduction band minimum (E_c) and valence band maximum (E_v) of the ZnS shell are more negative than those of the ZnO core, and both have the same valence charge balance. Hence, it was expected that a ZnS/ZnO heterojunction could facilitate the efficient separation of photoexcited electron–hole pairs. Heterojunction core/shell composites of ZnS film/ZnO NR were selected in this study to investigate their efficiency of separating excited electron–hole pairs.

Therefore, in this study, the photocatalytic performance of PANI-coated ZnS/ZnO heterojunctions was systematically studied. The role of PANI as a visible light sensitizer and as a prevention layer for photocorrosion, as well as that of the hybrid heterojunction as an efficient separation and transfer system for photoexcited electrons and holes, was investigated by microstructural characterization, UV-vis spectroscopy/X-ray photoelectron spectroscopy (XPS) measurements, and photoresponse analysis.

Experimental

Preparation of the ZnO NR/FTO glass photoelectrode

ZnO NRs were grown on FTO (resistance = 8 Ω m) glass by potentiostatic electrodeposition.[39,40] The FTO glass was placed in an aqueous solution of 0.5 mM $ZnCl_2$ (≥98%) and 0.1 M KCl (99%) under oxygen bubbling in a three-electrode electrochemical cell with a Pt mesh counter-electrode and a Ag/AgCl/sat. KCl reference electrode. Electrodeposition was carried out at −1.0 V for ∼3 h at room temperature.

Particulate ZnS film coating on ZnO NRs

A particulate ZnS film was coated on the surface of the ZnO NRs by immersing the ZnO NR electrode in an aqueous 0.32 M $Na_2S{\cdot}9H_2O$ (≥98%) solution for ∼12 h. Sulfurization by an anion-exchange reaction was carried out in a deionized water bath at 60 °C. $Na_2S{\cdot}9H_2O$ was used as an S^{2-} anion source to form ZnS on the surface of the ZnO NRs, according to the following reaction:

$$ZnO_{(s)} + S_{(aq)}^{2-} + H_2O_{(l)} = ZnS_{(s)} + 2OH_{(aq)}^{-}$$

The electrode was then washed with deionized water and absolute ethanol (≥99.8%) several times and dried at 80 °C for 2 h in an oven.[41,42]

PANI sensitizer coating on particulate ZnS film/ZnO NR

The PANI sensitizer was coated by successive ionic layer adsorption and reaction using ammonium persulfate as an oxidizing agent. First, 0.4 M aniline (≥99%) was dissolved in 1 M sulfuric acid (95–98%), which served as a cationic precursor in the first beaker. The second beaker contained an oxidant solution of 0.2 M ammonium persulfate (≥98%) in 1 M sulfuric acid, which served as an anionic precursor. The electrodes were then immersed into the aniline solution for 60 s for the surface polymerization of PANI on the particulate ZnS film/ZnO NR. Subsequently, the electrodes were immersed in the ammonium persulfate solution for 30 s.[43,44]

Microstructural characterization

The microstructure of the photoelectrodes was characterized by field-emission scanning electron microscopy (FE-SEM; JSM-6500 F, JEOL), field-emission transmission electron microscopy (FE-TEM; 200 kV/JEM-2100F HR, JEOL), and X-ray diffraction (XRD, SWXD, Rigaku). Ultraviolet-visible (UV-vis) absorbance spectra of the electrodes were obtained using an ultraviolet-visible-near infrared (UV-vis-NIR) spectrophotometer (UV 2600, Shimadzu). XPS was performed using a Thermo VG ESCALAB 250 instrument equipped with a microfocused, monochromatic A1 K_α X-ray source (1.486.6 eV) and a magnetic lens. The X-ray spot size was 500 μm (15 kV, 150 W). The spectra were acquired in constant analyzer energy mode with a pass energy of 150 eV and 40 eV for overview scans and high-resolution scans, respectively.

Photoelectrochemical characterization

The photocurrent densities of the photoelectrodes were measured using a potentiostat (AMT VERSASTAT 3, Princeton Applied Research) and a three-electrode cell with Pt mesh as the counter electrode and Ag/AgCl/sat. KCl as the reference electrode separated by a proton exchange membrane in aqueous 0.5 M Na_2SO_4 (pH = 7.15) electrolyte. Using a 1 kW xenon lamp (Newport) with the infrared wavelengths filtered out by water, 1 cm^2 of the

working electrode was exposed. The light irradiance, measured using a thermopile detector, was 100 mW cm^{-2}.

Results and discussion

In this study, the photocatalytic properties of ZnS film/ZnO NR heterojunctions with PANI layers were investigated. For heterojunction composite fabrication, after ZnO NRs were grown on FTO substrates by electroplating, ZnS layers were formed *via* sulfurization followed by PANI coating *via* cationic surface polymerization. Cross-sectional and surface FE-SEM images of the ZnO NRs (Fig. 1) show that hexagonal ZnO NRs with diameters of 300–500 nm and lengths of 0.5–1.5 μm were grown vertically.

The top surface of the prepared ZnO NRs is dominated by slanted side faces of $\{10\bar{1}1\}$ crystal planes rather than flat hexagonal {0001} crystal planes. Compared to those of hexagonal {0001} planes, $\{10\bar{1}1\}$ crystal planes have lower stacking density and thus higher surface energy. The hydrothermal growth rate of ZnO NRs on FTO is determined primarily by the diffusion rate of Zn^{2+} ions during the process, and ion diffusion into side $\{10\bar{1}1\}$ planes is much more than that into top {0001} surfaces, such that the hydrothermally grown ZnO NRs show wide {0001} crystal planes on their top surfaces. On the other hand, electroplated ZnO NRs have narrow and sharp top surfaces composed of hexagonal {0001} planes, because the Zn^{2+} concentration is much higher near the top surfaces due to the higher electroplating potential.[45–48] However, many voids are observed on the surface of ZnO NRs (Fig. 1), probably formed by O_2 gas bubbles in the electroplating bath which disturb the migration of Zn^{2+} ions on the surface. Meanwhile, for fabrication of heterojunction composites with efficient charge separation, ZnS films were coated on the surface of the ZnO NRs *via* ion exchange sulfurization. When the ZnO NRs were dipped in Na_2S solution, the O^{2-} ions on the ZnO surface and the S^{2-} ions in the Na_2S solution were exchanged to form ZnS particles on the surface of the ZnO NRs. Cross-sectional and surface images of the ZnS film/ZnO NR fabricated by this process are shown in Fig. 1(c) and (d). As shown in Fig. 1(d), the ZnS films consist of stacked agglomerates of ~25 nm nanoparticles. Cross-sectional and top surface images of the conductive organic sensitizer PANI, coated on the ZnS film/ZnO NR, are shown in Fig. 1(e) and (f), respectively. As shown in Fig. 1(f), the smooth surface of a ZnO NR is surrounded by both ZnS film composed of stacked agglomerated nanoparticles and PANI film.

TEM images of PANI/ZnS film/ZnO NR (Fig. 2(a) and (b)) show that a core electrodeposited ZnO NR is surrounded by both ~5 nm-thick PANI film and ~30 nm-thick particulate ZnS film. Thus, this core/shell structure should prevent direct contact of ZnO NRs with the electrolyte in the photocatalytic cells, preventing deterioration of the photocatalytic current due to photocorrosion. ZnS films on ZnO NRs can typically be formed by several methods such as chemical absorption of ZnS nanoparticles and vapor–liquid–solid (VLS) methods. However, for direct adhesion of ZnS nanoparticles on the ZnO surface, micro-voids can occur in the sites between the ZnS nanoparticles. Lattice mismatch between the ZnS nanoparticles and ZnO NRs can also cause interface defects. Thus, annealing processes are necessary to minimize these crystalline defects. In VLS methods using Zn and S powder sources, non-uniform adsorption of Zn and S vapors on the surface of ZnO NRs, which have different surface states depending on the crystal orientation, results in anisotropic growth of ZnS. Thus, it is difficult to obtain dense ZnS films using this technique, but thick films can be obtained. In surface sulfurization processes, however, uniform ZnS films can feasibly be formed, because ZnS nanoparticles are formed by ion exchange of O^{2-} ions on the ZnO surface and S^{2-} ions in the solution. Furthermore, the crystal orientation of ZnO NRs has a negligible effect on the growth of ZnS because the ZnO surface is surrounded by water molecules in the solution. The PANI film synthesized by polymerization was deposited relatively uniformly on the ZnS film. Selected area electron diffraction patterns for the interface between the particulate ZnS film and ZnO NRs are shown in Fig. 2(c). Polycrystalline ring patterns and single-crystalline dot patterns

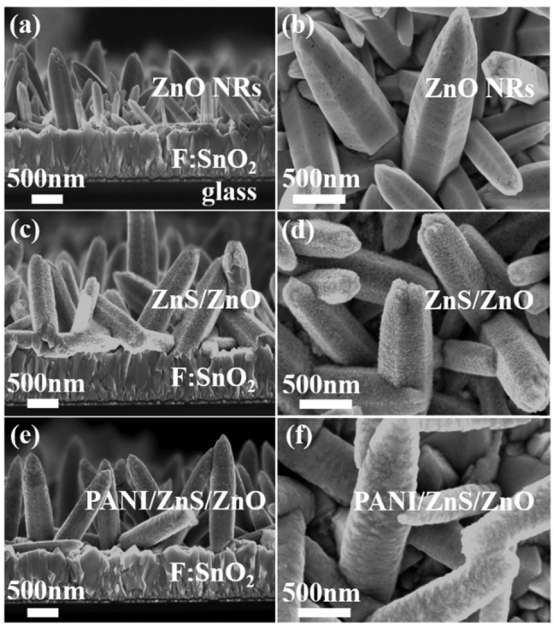

Fig. 1 FE-SEM images of coated PANI on a sulfurized ZnO NR core. Cross sectional and surface views of (a and b) ZnO NR/FTO; (c and d) particulate ZnS film/ZnO NR/FTO; and (e and f) PANI/particulate ZnS film/ZnO NR/FTO, respectively.

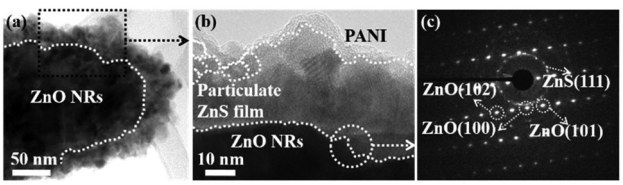

Fig. 2 TEM (a) bright field and (b) lattice fringe images of PANI/particulate ZnS film/ZnO NR, and (c) selective area electron diffraction pattern of the interface between the particulate ZnS film and ZnO NRs.

are observed for the particulate ZnS film and the ZnO NRs, respectively. Electron diffraction patterns from (100), (101), and (102) ZnO (zincite space group *P*63*mc*; JCPDS card no. 36-1451) for the [0$\bar{1}$0] zone axis are observed, confirming the hexagonal Wurtzite structure of the ZnO NRs. However, the electron diffraction patterns of the ZnS film correspond to both the (111) sphalerite cubic phase (space group *F*43*m*; JCPDS card no. 05-0566) and the (008) hexagonal phase (space group *P*63*mc*; JCPDS card no. 39-1363), which have interplanar distances of 3.123 Å and 3.120 Å, respectively. At this point, the structure of ZnS is not clear. However, other groups using similar ZnS synthesis processes reported cubic zinc blende (111) peaks at $2\theta = 28.62^{\circ}$ in XRD patterns.

The XRD patterns for PANI/particulate ZnS film/ZnO NR/FTO samples (Fig. 3) indicate that the peaks ($2\theta = 31.8^{\circ}$, 34.5°, 36.3°, 47.6°, 56.5°, and 62.9°) of the ZnO NRs correspond to the (100), (002), (101), (102), (110), and (103) crystal planes, respectively, of the hexagonal crystal lattice of zincite (space group *P*63*mc*; JCPDS card no. 36-1451). The peak at $2\theta = 28.61^{\circ}$ corresponds to the cubic ZnS(111) crystal plane. However, XRD peaks for the PANI layer are not observed. This is due to the amorphous phase of the PANI layer after the synthesis and dip-coating, whereas another group has reported polycrystalline PANI synthesis. This discrepancy is attributed to different processes including sources for the PANI synthesis.[49]

A compositional surface analysis of the PANI layer and ZnS film/ZnO NR was carried out using X-ray photoelectron spectroscopy (XPS), and the analysis results are shown in Fig. 4. Zn $2p_{1/2}$ (1045 eV), Zn $2p_{3/2}$ (1020 eV) and O 1s (531 eV) peaks were observed for the ZnO NRs, and S 2s (226 eV) and S 2p (162 eV) peaks were observed for the ZnS films. On the other hand, N 1s (399 eV) and C 1s (285 eV) peaks were observed for PANI. The N 1s (399 eV) peak, consisting of imine R3-N = C-R1R2 (398.5 eV), amine R1R2-NH (399.7 eV), and protonated nitrogen $-N^{+}$ = (401.9 eV) signals, originates from the N element of the aniline monomer, as shown in Fig. 4(b).[50]

UV-vis absorption spectra of PANI/ZnS film/ZnO NR, ZnS film/ZnO NR, and ZnO NR electrodes were measured and are shown in Fig. 5(a). All spectra show strong absorption in the UV region between 360 and 380 nm. The bandgaps of each layer were estimated from Tauc plots as shown in Fig. 5(b).[51] The values from the line intersections were measured as 3.12, 3.16, and 2.7 eV for ZnO NRs, ZnS film/ZnO NR, and PANI/ZnS film/ZnO NR, respectively. The ZnO NRs coated with a ZnS film of a wide bandgap showed a slightly increased bandgap, which is called blue-shifted absorption. However, wide and weak absorption in the visible region between 400 and 500 nm was observed for the PANI-coated ZnS film/ZnO NR sample. This resulted in a reduced bandgap of 2.7 eV in the Tauc plot. This is due to the narrow bandgap of the PANI layer in the range of 2.4–2.8 eV.[52]

The photocurrent densities of the samples were measured in a photoelectrochemical (PEC) cell under exposure to white light consisting of UV and visible light (see Fig. 6(a)). The photocurrent density corresponding to the pure photoresponse was measured by using an on–off chopped light source. The measured photocurrent density was the photoresponse difference between the on- and off-states of the light source. Under white light illumination, representative photocurrent densities of ZnO NRs, ZnS film/ZnO NR, and PANI/ZnS film/ZnO NR were

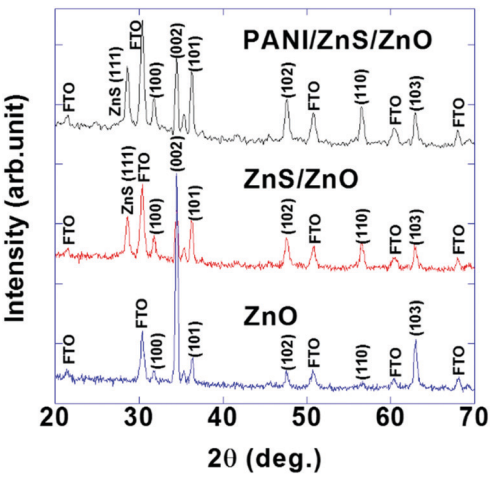

Fig. 3 X-ray diffraction patterns of PANI/particulate ZnS film/ZnO NR, ZnS/ZnO NR, and ZnO NRs on FTO glass.

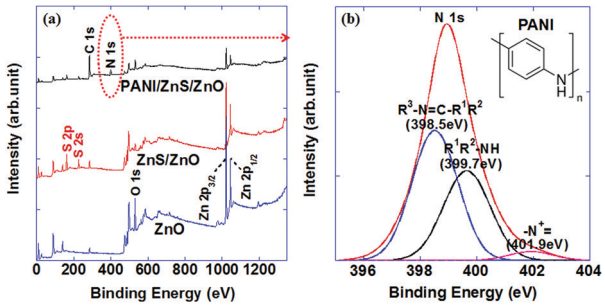

Fig. 4 XPS spectra of (a) PANI/particulate ZnS film/ZnO NR, particulate ZnS film/ZnO NR, and ZnO NRs; and (b) chemical element N 1s peak composed of imine as R3–N═C-R1R2 (398.5 eV), amine as R1R2-NH (399.7 eV), and protonated nitrogen as $-N^{+}$ = (401.9 eV).

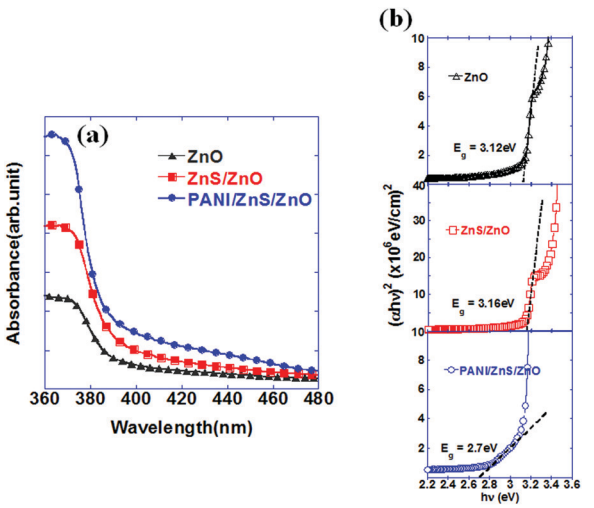

Fig. 5 (a) UV-vis absorption spectra and (b) Tauc plots for bandgap calculations of ZnO NR, ZnS film/ZnO NR, and PANI/ZnS film/ZnO NR electrodes.

0.173, 0.461, and 0.865 mA cm^{-2}, respectively, at 0.5 V. The PANI/ZnS film/ZnO NR electrode showed about 5 and 1.8 times larger photocurrent density than the ZnO NRs and ZnS film/ZnO NR, respectively. The ZnS film/ZnO NR electrode showed about 2.7 times larger photocurrent density than the ZnO NRs. These measurement results confirm the light absorption spectral analysis results (Fig. 5). The photocurrent density of PANI/ZnS film/ZnO NR was significantly improved due to superior visible light absorption by the PANI layers. The bandgap of PANI/ZnS film/ZnO NR is 2.7 eV, as shown in Fig. 5(b), compared to 3.16 eV for ZnS film/ZnO NR and 3.12 eV for ZnO NRs. Meanwhile PANI has prevented ZnS and ZnO photocorrosion, which reduces the photocurrent density. Furthermore, both the PANI/ZnS film/ZnO NR and ZnS film/ZnO heterojunctions have a good enough combination of potential levels (see the energy band alignment of Fig. S1, ESI†) to transfer and efficiently separate excited electrons and holes.[53–56] That is, the CB and VB energy levels are in the order: $CB_{PANI} > CB_{ZnS} > CB_{ZnO}$, $VB_{PANI} > VB_{ZnS} > VB_{ZnO}$. This means that electron transfer can occur from PANI to ZnS and ZnS to ZnO, and hole transfer from ZnO to ZnS and ZnS to PANI. The data presented in Fig. 6(a)–(c) allow determination of the photoconversion efficiency, η:[57]

$$\eta = \frac{I(1.23 - V_B)}{I_R S}$$

where I is the measured photocurrent density, V_B is the applied bias, I_R is the solar radiation intensity, and S is the exposure area. Fig. 6(d) shows the photoconversion efficiency as a function of applied bias V_B. PANI/ZnS film/ZnO NR shows an efficiency of 0.71%, much higher than those for ZnS/ZnO (0.34%) and ZnO (0.17%). This means that PANI contributes to visible light absorption and prevention of photocorrosion of ZnS film/ZnO NR.

Fig. 7(a) shows the kinetics of photocurrent density changes corresponding to successive sudden switching on and off of white light for PANI/ZnS film/ZnO NR, ZnS film/ZnO NR, and ZnO NRs. The characteristic extremes (maximum and minimum for light on and light off, respectively) are clearly visible in Fig. 7(a) and may be described in terms of two competitive processes: generation of electron–hole pairs and their recombination. The process of recombination is controlled by the following kinetic equation:

$$D = \exp\left(-\frac{t}{\tau}\right)$$

where D is defined as

$$D = \frac{I(t) - I(\mathrm{f})}{I(\mathrm{i}) - I(\mathrm{f})}$$

and t denotes time, τ is a parameter defined as the transient time constant, I is either photoanodic current, and i and f are related to the initial and final (steady state) states. The physical meanings of both I(i) and I(f) are shown in Fig. S2 (ESI†). Fig. 7(b) illustrates ln D *vs.* time for PANI/ZnS film/ZnO NR, ZnS film/ZnO NR, and ZnO NRs. The determined transient time constant of the PANI/ZnS film/ZnO NR photoelectrode is about eight times and nine times higher than that of the ZnS film/ZnO NR and ZnO NRs, respectively. It means that ZnS film/ZnO NR and ZnO NRs lead to an increase of the recombination process and photocorrosion reaction where excited electron–hole pairs are consumed. It is well known that the self-redox potential level located in their bandgap increases photocorrosion.[58]

In summary, PANI/ZnS film/ZnO NR photoelectrodes were fabricated and evaluated for their photocatalytic performance. Single-crystalline hexagonal ZnO NRs of lengths 0.5–1.5 μm were grown on FTO glass. Cubic ZnS films consisting of 5–10 nm nanoparticles were coated with a thickness of ~30 nm on the ZnO NRs, and organic PANI layers with a thickness of ~5 nm were coated on the ZnS films. XRD and XPS analyses showed strong peaks corresponding to the ZnS(111) and ZnO(002) crystal planes, and the C/N elements and molecular bonding structure were observed for PANI.

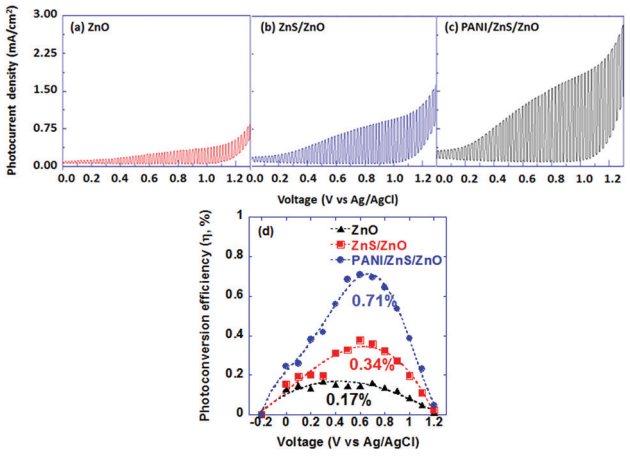

Fig. 6 Photocurrent density of (a) ZnO NR, (b) ZnS film/ZnO NR, and (c) PANI/ZnS film/ZnO NR electrodes under white light (UV and visible light) irradiation; (d) the photoconversion efficiency is calculated using the photocurrent density.

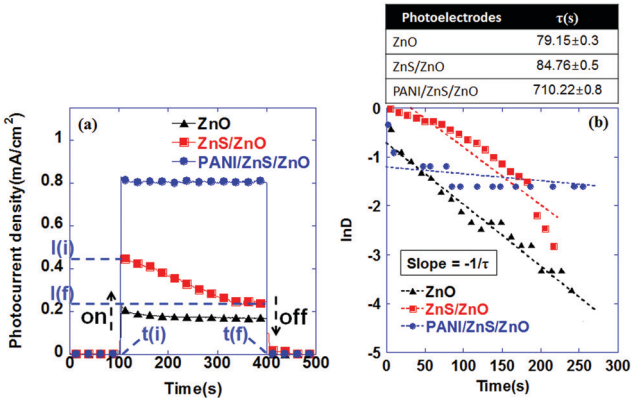

Fig. 7 (a) Kinetics of the photocurrent density of biased (V = 0.5 V) electrodes and (b) normalized plot of the photocurrent density–time dependence for ZnO, ZnS/ZnO, and PANI/ZnS/ZnO.

Conclusions

Photoelectrodes of PANI-coated ZnS film/ZnO NR heterojunctions on FTO glass were evaluated for their photocatalytic performance. Under white light illumination, the PANI/ZnS film/ZnO NR electrode showed approximately 5.0 times higher photocurrent density than ZnO NRs. This was attributed to the superior properties of the PANI layers, which absorb visible light and prevent photocorrosion, and also provide proper energy band alignment of the hybrid heterojunction (PANI/ZnS film/ZnO NR) to efficiently transfer and separate excited electrons and holes. It is expected that this hybrid heterojunction photoelectrode with proper band alignment using organic materials could be utilized for other applications such as photovoltaics, solar CO_2 fuel conversion, and solar pollutant decomposition.

Conflicts of interest

There are no conflicts to declare.

Acknowledgements

This research was supported by the Space Core Technology Development Program through the National Research Foundation of Korea (NRF) funded by the Ministry of Education Science and Technology (MEST) (2017M1A3A3A02016666).

Notes and references

1 Y. Lan, Z. Liu, Z. Guo, X. Li, L. Zhao, L. Zhan and M. Zhang, *Dalton Trans.*, 2018, **47**, 12181–12187.
2 D. Chen, Z. Liu, Z. Guo, W. Yan and Y. Xin, *J. Mater. Chem. A*, 2018, **6**, 20393–20401.
3 Z. Liu, Q. Song, M. Zhou, Z. Guo, J. Kang and H. Yan, *Chem. Eng. J.*, 2019, **374**, 554–563.
4 Y. Li, Z. Liu, J. Zhang, Z. Guo, Y. Xin and L. Zhao, *J. Alloys Compd.*, 2019, **790**, 493–501.
5 D. Chen and Z. Liu, *ChemSusChem*, 2018, **11**, 3438–3448.
6 Z. Wang and L. Wang, *Sci. China Mater.*, 2018, **61**, 806–821.
7 Y. He, T. Hamann and D. Wang, *Chem. Soc. Rev.*, 2019, **48**, 2182–2215.
8 A. Eftekhari, V. J. Babu and S. Ramakrishna, *Int. J. Hydrogen Energy*, 2017, **42**, 11078–11109.
9 B. Liu, Y. Fang, Z. Li and S. Xu, *J. Nanosci. Nanotechnol.*, 2015, **15**, 889–920.
10 A. A. Valeeva, E. A. Kozlova, A. S. Vokhmintsev, R. V. Kamalov, I. B. Dorosheva, A. A. Saraev, I. A. Weinstein and A. A. Rempel, *Sci. Rep.*, 2018, **8**, 1–10.
11 C. Li, H. Wang, S. B. Naghadeh, J. Z. Zhang and P. Fang, *Appl. Catal., B*, 2018, **227**, 229–239.
12 S. Kumar, S. Karthikeyan and A. F. Lee, *Catalysts*, 2018, **8**, 1–47.
13 L. Tian, Y. Rui, K. Sun, W. Cui and W. An, *Nanomaterials*, 2018, **8**, 1–13.
14 S. Ni, T. Zhou, Y. Zhu, Y. Cao and P. Yang, *Bull. Mater. Sci.*, 2018, **41**, 1–8.
15 S. Velanganni, S. Pravinraj, P. Immanuel and R. Thiruneelakandan, *Physica B*, 2018, **534**, 56–62.
16 N. X. Sang, T. T. Tung, P. T. L. Huong, N. H. Tho and D. Losic, *J. Phys. D: Appl. Phys.*, 2018, **51**, 1–24.
17 S. Rampino, F. Pattini, M. Bronzoni, M. Mazzer, M. Sidoli, G. Spaggiari and E. Gilioli, *Sol. Energy Mater. Sol. Cells*, 2018, **185**, 86–96.
18 Y. Cai, J. Song, X. Liu, X. Yin, X. Li, J. Yu and B. Ding, *Environ. Sci.: Nano*, 2018, **5**, 2631–2640.
19 C. Ye, Y. Zhang, A. Ding, Y. Hu and H. Guo, *Sci. Rep.*, 2018, **8**, 1–6.
20 A. B. Athanas, S. Thangaraj and S. Kalaiyar, *Chem. Phys. Lett.*, 2018, **699**, 32–39.
21 S. Ouedraogo, B. Chouchene, C. Desmarets, T. Gries, L. Balan, R. Fournet, G. Medjahdi, K. Bayo and R. Schneider, *Appl. Catal., A*, 2018, **563**, 127–136.
22 M. Z. Rahaman and A. K. M. A. Hossain, *RSC Adv.*, 2018, **8**, 33010–33018.
23 Y. Yang, L. C. Yin, Y. Gong, P. Niu, J. Q. Wang, L. Gu, X. Chen, G. Liu, L. Wang and H. M. Cheng, *Adv. Mater.*, 2018, **30**, 1–8.
24 N. Kirkwood, J. O. V. Monchen, R. W. Crisp, G. Grimaldi, H. A. C. Bergstein, I. D. Fossé, W. V. D. Stam, I. Infante and A. J. Houtepen, *J. Am. Chem. Soc.*, 2018, **140**, 15712–15723.
25 A. N. Singh, H. Devnani, S. Jha and P. P. Ingole, *Phys. Chem. Chem. Phys.*, 2018, **20**, 26719–26733.
26 F. Nan, P. Li, J. Li, T. Cai, S. Ju and L. Fang, *J. Phys. Chem. C*, 2018, **122**, 15055–15062.
27 Y. Wu, P. Wang, X. Zhu, Q. Zhang, Z. Wang, Y. Liu, G. Zou, Y. Dai, M. H. Whangbo and B. Huang, *Adv. Mater.*, 2018, **30**, 1–6.
28 D. B. Potter, M. J. Powell, I. P. Parkin and C. J. Carmalt, *J. Mater. Chem. C*, 2018, **6**, 588–597.
29 B. Bajorowicz, E. Kowalska, J. Nadolna, Z. Wei, M. Endo, B. Ohtani and A. Medynska, *Dalton Trans.*, 2018, **47**, 15232–15245.
30 Y. Chen, G. Tian, W. Zhou, Y. Xiao, J. Wang, X. Zhang and H. Fu, *Nanoscale*, 2017, **9**, 5912–5921.
31 S. Muthulingam, K. B. Bae, R. Khan, I. Lee and P. Uthirakumar, *RSC Adv.*, 2015, **5**, 46247–46251.
32 M. Ates, *J. Adhes. Sci. Technol.*, 2016, **30**, 1510–1536.
33 F. Garnier and G. Horowitz, *Macromol. Symp.*, 1987, **8**, 159–170.
34 B. Weng, M. Qi, C. Han, Z. Tang and Y. Xu, *ACS Catal.*, 2019, **9**, 4642–4687.
35 H. Ghannam, C. Bazin, A. Chahboun and M. Turmine, *CrystEngComm*, 2018, **20**, 6618–6628.
36 L. Xu, Q. Liao, J. Zhang, X. Ai and D. Xu, *J. Phys. Chem. C*, 2007, **111**, 4549–4552.
37 M. Romero, R. Henríquez and E. A. Dalchiele, *Int. J. Electrochem. Sci.*, 2016, **11**, 8588–8598.
38 Y. Shirahata, K. Tanaike, T. Akiyama, K. Fujimoto, A. Suzuki, J. Balachandran and T. Oku, *AIP Conf. Proc.*, 2016, **1709**, 020018.
39 T. Frade, D. Siopa, A. F. Martins, J. F. C. Carreira, J. Rodrigues, N. B. Sedrine, M. R. Correia, T. Monteiro,

R. T. Zaera and A. Gomes, *J. Electrochem. Soc.*, 2018, **165**, D595–D603.
40 A. Burgos, R. Schrebler, G. Cáceres, E. Dalchiele and H. Gómez, *Int. J. Electrochem. Sci.*, 2018, **13**, 6577–6583.
41 C. H. Kao, W. M. Su, C. Y. Li, W. C. Weng, C. Y. Weng, C. C. Cheng, Y. S. Lin, C. F. Lin and H. Chen, *AIP Adv.*, 2018, **8**, 1–7.
42 N. K. Abbas, K. T. A. Rasoul and Z. J. Shanan, *Int. J. Electrochem. Sci.*, 2013, **8**, 3049–3056.
43 C. H. Park, S. K. Jang and F. S. Kim, *Appl. Surf. Sci.*, 2018, **429**, 121–127.
44 R. Karunagaran, C. Coghlan, D. Tran, T. T. Tung, A. Burgun, C. Doonan and D. Losic, *Materials*, 2018, **11**, 1–11.
45 M. Singh, X. Zhuo, D. S. Choi, L. E. Gonzalez, J. Wang and J. Hahm, *Nanosclae*, 2015, **7**, 18813–18826.
46 H. A. Wahab, A. A. Salama, A. A. E. Saeid, O. Nur, M. Willander and I. K. Battisha, *Results Phys.*, 2013, **3**, 46–51.
47 M. Singh, S. Song and J. Hahm, *Nanoscale*, 2014, **6**, 308–315.
48 M. Skompska and K. Zarebska, *Electrochim. Acta*, 2014, **127**, 467–488.
49 V. Talwar, O. Singh and R. C. Singh, *Sens. Actuators, B*, 2014, **191**, 276–282.
50 X. L. Wei, M. Fahlman and A. J. Epstein, *Macromolecules*, 1999, **32**, 3114–3117.
51 S. Awasthi, P. S. Gopinathan, A. Rajanikanth and C. Bansal, *J. Sci.: Adv. Mater. Devices*, 2018, **3**, 37–43.
52 A. S. Trevizo, P. A. Madrid, P. P. Ruiz, W. A. Flores and M. M. Yoshida, *Mater. Res.*, 2016, **19**, 33–38.
53 X. M. Shuai and W. Z. Shen, *J. Phys. Chem. C*, 2011, **115**, 6415–6422.
54 R. Li, Z. Wei, X. Fang, Y. Wang, Y. Li, D. Wang, J. Tang, D. Fang, X. Chu, B. Yao, R. Chen and X. Wang, *ACS. Appl. Nano. Mater.*, 2018, **1**, 1641–1647.
55 N. L. Marana, F. A. L. Porta, E. Longo and J. R. Sambrano, *Curr. Phys. Chem.*, 2015, **5**, 327–336.
56 M. Alam, N. M. Alandis, A. A. Ansari and M. R. Shaik, *J. Nanomater.*, 2013, 1–5.
57 M. Radecka, M. Wierzbicka, S. Komornicki and M. Rekas, *Physica B*, 2004, **348**, 160–168.
58 S. Chen and L. Wang, *Chem. Mater.*, 2012, **24**, 3659–3666.